# Tailoring nanodiamonds for high-contrast EPR imaging: size, surface properties, and spectroscopic performance

Sarah Garifo, Dimitri Stanicki, Thomas Vangijzegem, Philippe Mellet, Hugues A Girard, Jean-Charles Arnault, Sylvie Bégin-Colin, Yves-Michel Frapart, Robert N Muller, Sophie Laurent

# Tailoring Nanodiamonds for High-Contrast EPR Imaging: Size, Surface Properties and Spectroscopic Performance

Sarah Garifo[a], Dimitri Stanicki[a], Thomas Vangijzegem[a], Philippe Mellet[b,c], Hugues A. Girard[d], Jean-Charles Arnault[d], Sylvie Bégin-Colin[e], Yves-Michel Frapart[f], Robert N. Muller[a,g], Sophie Laurent[a,g*]

[a] NMR and Molecular Imaging Laboratory, General, Organic and Biomedical Chemistry Unit, University of Mons, B-7000 Mons, Belgium

[b] University of Bordeaux, CNRS, CRMSB, UMR 5536, F-33000 Bordeaux, France

[c] INSERM, F-33000 Bordeaux, France

[d] Université Paris-Saclay, CEA, CNRS, NIMBE, 91191 Gif sur Yvette, France

[e] UMR CNRS-UdS 7504, Institut de Physique et Chimie des Matériaux, CNRS, University of Strasbourg, 67034 Strasbourg, France

[f] University of Paris Cité, CNRS, LCBPT, F-75006 Paris, France

[g] Center for Microscopy and Molecular Imaging (CMMI), B-6041 Gosselies, Belgium

*Corresponding author. E-mail: sophie.laurent@umons.ac.be; Tel.: +32-65373594

**Keywords:** EPR imaging, nanodiamonds, nano-sized HPHT, air-annealing, Raman spectroscopy

## Abstract

Electron paramagnetic resonance (EPR) spectroscopy is a tool that provides sensitive detection of uncoupled electron spins for a variety of applications. This technique enables the specific detection and quantification of radical species, while also being able of generating high-contrast, background-free images. However, the EPR labeling and imaging techniques encounter limitations mainly due to the instability of organic radicals from organic probes, which can influence the reliability and scope of the experiment. In that context, the use of nanodiamonds (NDs) in EPR may be a promising route for understanding their unique properties and potential biomedical applications. The ability to perform EPR imaging in combination with the stable intrinsic properties of paramagnetic centers within these particles raises the possibility of extending nanodiamond-based imaging capabilities. Herein, we present a preliminary demonstration of a practical spectroscopy and imaging application using nanosized diamond particles (< 18 nm) for electron paramagnetic resonance imaging (EPRI). The discretization of two different nanodiamond production sources among the most studied NDs (HPHT or detonation), allows

further characterization of their physicochemical properties. In addition, we have investigated variations in the physicochemical properties of nanodiamonds, including size effects and surface treatments. Finally, we provide experimental evidence of the conditions required for optimal spectroscopic and imaging resolution ($R < 1$ mm) as well as achievable EPR sensitivity.

## Introduction

Electron paramagnetic resonance (EPR), as a spectroscopic technique, is specific to the resonance of paramagnetic species such as (in)organic radicals, complexes, crystallographic defects, colored centers or transition metal ions when subjected to a magnetic field. Many concepts in electron spin (or paramagnetic) resonance (ESR or EPR) spectroscopy are related to similar notions in nuclear magnetic resonance (NMR) spectroscopy [1]; likewise what NMR brings to MRI modality, EPR can enable EPR imaging (EPRI) using an additional magnetic field gradient in a set of different orientations around the sample. High-resolution images using a non-invasive imaging technique enable specific detection and quantification of paramagnetic species with optimal resolution. The choice of the probe depends on the specific application and the physicochemical properties of the sample under study [2]. Overall, the versatility and sensitivity of EPR probes make them essential tools for a wide range of applications in medicine, industry and environment. The best-known probes and their applications include: (i) nitroxides species for studying biological systems (*i.e.* superoxide spin trapping) [3,4], (ii) triarylmethyl radicals (TAM) for oximetry (*i.e.* to measure oxygen concentration in biological samples for in-depth assessment of tissue oxygenation, metabolism and redox evaluations) [5,6], or (iii) site-directed spin labeled (SDSL) nitroxides to evaluate structural and dynamic properties of organic systems, such as transmembrane transport and transcription mechanisms or as Cu(II) spin-labels [7–9]. However, the stability of paramagnetic organic compounds can be influenced by a number of factors such as pH, temperature or redox environment, influencing the reliability of the experiment. The probes, specifically tailored for paramagnetic labeling, can be assessed through EPR studies to obtain valuable information.

While we focus on the capabilities of EPR spectroscopy to analyze paramagnetic materials, a particular attention is paid to nanodiamonds (NDs), whose unique properties are attracting growing interest in a variety of scientific domains. Integrating the EPR properties of NDs into the EPR imaging modality enables in-depth characterization of these nanoplatforms, opening up new perspectives in applications ranging from nanomedicine to materials science. Indeed, nanodiamonds have emerged as promising carbon-based nanomaterials for a range of applications due to their unique advantages, particularly in the biological, medical and imaging fields

[10–12]. In these fields, the nitrogen-vacancies (NV) centers embedded in the core of the NDs are exploited for their ultra-stable fluorescence properties, while some of the fluorescent probes are limited either by their photostability or cytotoxicity [13–15]. Other interests include the use of crude NDs as non-cytotoxic substrates for gene and drug delivery [11,16], implants [17], tissue engineering or as powerful theranostic substrates for the targeted delivery of vaccines [18], chemotherapy agents [16,19], immunotherapeutics, Gd- and Mn-doped (grafted) DND MRI contrast agents [20–24] or for hyperpolarization MRI [25–28] using ND intrinsic impurities.

Apart from optical fluorescence, NMR or hyperpolarization purposes, options for non-invasive *in vitro* and *in vivo* imaging of nanodiamonds are very limited. Three main advantages of using NDs in EPRI can be noted; the first one is closely linked to the relative stability of the radical-like paramagnetic centers (in the bulk and the core of the particle), compared with conventional organic radicals (*i.e.* easy reduction through metabolic pathways) [29]. The second results from the nanoparticle unique characteristics; nanoparticles provide a versatile platform that can be used in a variety of biomedical and technological applications regarding their distinct physicochemical properties (enhanced surface area, properties tailoring, biocompatibility, tunable surface chemistry, surface charge or versatility) [30]. The third results from the EPR signal; the EPR signal of NDs typically exhibits narrow line indicating well-defined electron spin states resulting in a high signal to noise ratio (as a function of linewidth). In addition, the EPR spectrum may display other specific features corresponding to (structural) defects or impurities in the diamond lattice, depending on the material studied (nanodiamonds source, size, surface graphitization, crystallinity).

Two primary methods for producing nanoscale diamond particles have been introduced based on their production procedures; (i) a detonation-based synthesis where the carbon source is derived from the explosives or (ii) a mechanical grinding of high-quality HPHT (high-pressure high-temperature) diamond microcrystals into nanometric particles. Particles obtained by detonation are rather small (< 10 nm) and relatively monodisperse but exhibit poor crystalline quality, whereas those obtained by fragmentation of bulk material exhibit superior crystallinity, albeit with a broader size distribution (from hundreds of micrometers to a few nanometers) [31,32]. Depending on the nanodiamond synthesis procedure, their properties (size, structure, surface composition, EPR or optical luminescence properties and crystallinity) can be significantly impacted. For example, there are many more defects in $ND_{DET}$ compared to $ND_{HPHT}$ as a result of the uncontrolled explosion event. These include vacancies, dislocations, domain boundaries and amorphous carbon impurities, mainly on the surface and within the interface layer (*i.e.*

dangling bonds) [31,32]. In contrast, $ND_{HPHT}$ defects consist of vacancies, dislocations or stacking faults in a crystalline lattice. Furthermore, their surface properties are very different, with $ND_{DET}$ having a complex surface with a higher density of defects, amorphous and graphitic carbons, and various functional groups, leading to aggregation due to weak electrostatic interactions [31,32].

Ultimately, the choice between both types depends on specific requirements such as particle size distribution, purity, surface chemistry, or fluorescence stability. In general, small-sized detonation nanodiamond is the typical choice for MRI imaging purpose while larger size HPHT particles are suitable in tissue engineering or luminescence purpose [33].

Here, we present the physicochemical property variations from production source, size and surface treatments effects and EPR investigation. By means of mathematical developments, imaging optimizations and a reliable nanodiamond strategy, we demonstrate EPRI capabilities using this nanomaterial. To our knowledge, it is the first experimental evidence of EPR imaging using NDs.

## Materials and methods

### Materials

Monocrystalline synthetic microdiamond powder of HPHT origin (Microdiamant MSY 0 – 0.03) was supplied by Pureon AG (Lengwil, Switzerland). Primary particles of detonation nanodiamond were manufactured by NanoAmando® (NanoCarbon Research Institute Ltd., Nagano, Japan). Branched poly(ethyleneimine) (MW = 1,200 Da, $\geq$ 99%) and ICP zirconium plasma standard were supplied by ThermoFischer Scientific (Merelbeke, Belgium). ICP multi-element standard solution was supplied by Merck (Hoeilaart, Belgium). All chemicals used were of standard purity grade. Stirred cells and membranes (MWCO = 100 kDa, RC) for ultrafiltration were purchased from Metrohm (Antwerpen, Belgium).

### Preparation of nanodiamond suspensions

Nanodiamond suspensions were prepared by dispersing diamond powders (200 mg) either used as-received (written "$asrec$") or thermally oxidized (written "ox") in deionized (DI) water. To ensure a good colloidal dispersion, particles were sonicated in DI water for 90 minutes (10-min steps) using a ultrasound probe (Hielscher, 200 W, 24 kHz) with an amplitude of 70% (duty cycle: ½) and slightly centrifuged (670 g, 5 minutes) to exclude larger aggregates. Nanoparticle density was obtained gravimetrically after freeze-drying 1 mL of the suspension followed by a

drying step at 80°C for 24 hours. If necessary, nanodiamonds were concentrated by stirred ultrafiltration cell device (MWCO = 100 kDa) to reach a particle concentration of 20 mg $mL^{-1}$.

**Oxidative treatment by air-annealing**

A ceramic crucible filled with crude freeze-dried diamond powder was heated in a muffle furnace (heating rate: 10°C $min^{-1}$) in air at 400°C (written "ox-1"), 450°C (ox-2), 480°C (ox-3) or 550°C (ox-4) for 4 hours (Nabertherm GmbH, Lilienthal, Germany) to remove the graphitic shell and modify oxidation-sensitive chemical groups. The conditions of oxidative air treatment by air-annealing were studied by thermal analysis (TGA) and carried out in accordance with published procedures with some modifications [34,35]. The air-annealed (oxidized) NDs were then dispersed in DI water as previously described to obtain a gray/black -colored nanodispersion (20 mg $mL^{-1}$).

**Size exclusion process**

Sub-17 nm $ND_{HPHT}$ fractions were obtained by successive high-speed centrifugation cycles on $ND_{HPHT}^{asrec}$ (5 mg $mL^{-1}$). Between each centrifugal treatment (IEC CL31R Multispeed Centrifuge, 16,800 g; $0 < n < 7 \times 60$-min steps), the supernatant was carefully isolated, characterized and treated again. Their notations throughout the article are written as followed: $ND_{HPHT}^{1}$ isolated after a centrifugation cycle of 1 × 60 min; $ND_{HPHT}^{2}$ sample isolated after 2 × 60 min, etc. This procedure was not applied to detonation nanodiamonds due to a lack of colloidal stability resulting from their aggregation state.

**Physicochemical characterization techniques**

Hydrodynamic particle size and zeta potential were determined by photon correlation spectroscopy (PCS) using a Zetasizer Nano ZS particle size analyzer (Malvern Instruments, He-Ne laser, 633 nm, scattering angle 173°) (Worcestershsire, UK) on diluted suspensions (1 mg $mL^{-1}$ in DI water, 25°C). The refractive index of bulk diamond (2.4 at 635 nm) was used to evaluate intensity and number -weighted distributions. PCS measurements are presented as mean values (hydrodynamic $D_H^{PCS}$ or number diameters, $D_{\#}^{PCS}$ and zeta potential, $\zeta$) ± standard deviation. The evolution of zeta potential was investigated in relation to pH changes; the pH of each nanodiamond sample was adjusted using diluted $HNO_3$ or TMAOH solution.

TEM experiments were performed with a Fei Tecnai 10 electron microscope (Oregon, USA) operating at an accelerating voltage of 80 kV under vacuum in order to obtain detailed information on the morphology and the size distribution of a sample. Each specimen was prepared following a procedure slightly adapted from Rehor *et al.* [36]. Briefly, 300 mesh carbon-

coated formvar grids (Ted Pella Inc, California, USA) were pretreated using an UV/ozonizing chamber (AppliTek scientific instruments, Nazareth, Belgium) for 15 min. A mixture droplet (4 µL) of a branched ethyleneimine polymer solution (MW = 1,2 kDa, 0.1 mg $mL^{-1}$) and a 0.1 mg $mL^{-1}$ colloidal suspension was then placed on the grid allowing the liquid to dry in air at room temperature. The statistical particle size distribution was obtained by examining multiple images of each sample using iTEM software (Münster, Germany) using the Feret diameter as size expression due to the irregular shape of the studied $ND_{HPHT}$ particle. By measuring the diameter size over 400 to 500 counted particles for each sample, the mean equivalent median diameter ($D^{TEM}$), the polydispersity index ($PDI^{TEM}$) and a standard deviation (SD) from the corresponding particle suspension were calculated [37]. A size histogram showing the number-weighted distribution was obtained and the resulted histograms were fitted with a log-normal function.

Thermogravimetric analyses (TGA) were acquired on a TA Q500 device (TA Instruments, New Castle, USA). The mass loss of pre-dried HPHT and DET samples monitored under air was over the process for thermal stability investigation. After an isotherm at 120°C for 10 minutes (heating rate: 10°C $min^{-1}$), the temperature was increased from 120 to 800°C at a heating rate of 10°C $min^{-1}$ under air flow (25 mL $min^{-1}$) and the temperature was maintained for 5 minutes.

The Boehm titration method was evaluated on $ND_{DET}^{asresc}$, $ND_{DET}^{ox-1}$ and $ND_{HPHT}^{asresc}$ nanoparticles (10 mg $mL^{-1}$) under conductometric detection (SI Analytics, Lab 945, Xylem) to quantify the oxygenated functional groups present on the particle surface according to a published procedure [38].

Infrared spectra (ATR) of dried powders were recorded on a PerkinElmer FT-IR Spectrum 100 spectrometer (Manchester, UK) with an average of 4 scans and a resolution of 4 $cm^{-1}$.

Raman measurements were performed on a Xplora Raman spectrometer (Horiba) under green wavelength laser excitation (532 nm, 0.79 mW) equipped with a 1800 tr/mm grating. *Prior* to their characterizations, samples were dispersed in DI water and dispensed onto a Si substrate by drop-casting for analysis. Spectra has been recorded with a 10 s acquisition time, repeated 10 times. To ensure the representativeness of the spectra presented here, three different areas of the samples were systematically probed.

The surface chemistry of the nanodiamond samples was characterized by X-ray photoelectron spectroscopy (XPS) using a XPS Versa Probe Phi 5000 spectrometer (Chanhassen,

USA). The X-ray source was a monochromatized Al Kα line ($E_b$ = 1,486.7 eV). Measurement of the deconvoluted *C1s* and *O1s* orbitals peaks energies were carried out using a linear baseline and Gaussian line curves of variable widths.

The elemental composition of the nanodiamonds was determined by high-resolution TEM energy-dispersive X-ray spectroscopy (HRTEM-EDX) scanning area with an average of three measurements for the qualitative measurements (TEM grids: Formvar/Carbon supported copper grids). *Prior* to quantitative analysis of impurities, the as-received detonation and HPHT powders (250.0 ± 0.1 mg) were calcinated in a muffle furnace (heating rate: 10°C minute$^{-1}$; 650°C for 3 hours) [39]. The resulting yellow/light brown residues (6.3 – 3.4 mg, respectively) were then quantitatively transferred into Teflon vessels for microwave acid digestion (Milestone MLS 1200 Mega, Analis, Belgium). A level of total uncalcinated impurities of 2.52%$_{w/w}$ and 1.36%$_{w/w}$ for DET and HPHT powders, respectively was measured gravimetrically, corresponding to 95 – 98% of major carbon element in NDs. The volumes of the resulting acid-treated samples were then adjusted to 25 mL using DI water. The impurities (*ie*. Ag, Al, Zn, Fe, Cr, Cu, Zr, Mn) content was quantified by inductively coupled plasma-atomic emission spectroscopy (ICP-AES) under argon plasma on a Varian Liberty Series II instrument (Varian Inc., Palo Alto, USA). Calibration curves ($R^2$ > 0.99) using different dilutions of an ICP multi-element standard solution were constructed to ensure proper quantifications of each metallic impurities.

**EPR spectroscopy and imaging**

*EPR spectroscopy.* X-band electron paramagnetic resonance spectroscopy was used to identify the paramagnetic contributions to the overall EPR spectrum and to obtain quantitative information on paramagnetic centers. Samples (20 mg mL$^{-1}$ in DI water) were analyzed at room temperature on a Bruker EMX nano (Bruker, Rheinstetten, Germany). The following spectroscopic parameters were used: 343.5 mT center field, the microwave frequency was ~ 9.8 GHz, the magnetic field modulation amplitude was 0.1 mT and frequency 100 kHz and presented as the derivative of the microwave absorption over the magnetic field. In the specific case of nanodiamonds, their EPR spectra typically present a single line characterized by a narrow or large resonant shape depending on the electron spin states. Therefore, the type of (isotropic) broadening applied to a linewidth (lw) is referred to as lwpp (pp, peak-to-peak) to measure the horizontal distance between the maximum and the minimum of the first-derivative EPR line shape. The *g*-factor refers to the spectroscopic splitting factor, characterizing the behavior of

species in a magnetic field and is extracted from the minima in the second-derivative EPR spectra.

*Spectroscopic simulation.* EPR spectra were simulated using EasySpin software package (Matlab) [40].

*Low frequency EPR settings.* Low micro-wave spectroscopic EPR data were recorded at 1 GHz (L-band) on a CW EPR E540L spectrometer (Bruker, Rheinstetten, Germany) at room temperature.

*Phantom preparation.* Nanodiamond suspensions in DI water (filled with 100 – 200 µL at a 10 mg $mL^{-1}$ particle density) were placed in EPR tubes (4 mm, 1 mm, 0.5 mm, 0.4 mm and 0.3 mm quartz capillary diameter size) inserted into a 23 mm birdcage resonator mounted inside the device for phantom imaging study.

*Phantom EPR imaging experiments.* The EPR imaging was performed using the L-band spectrometer [40]. The continuous wave system was equipped with gradient coils to obtain information about the spatial distribution of free radicals in nanodiamond samples. Spectrometer parameters were as followed: microwave power: 50 mW; field of view (FOV) diameter: 82.4 mm; sweep width: 8.24 mT; Microwave frequency: 1.105 GHz; amplitude modulation: 0.2 mT; frequency modulation: 50 kHz. Experimental resolutions were evaluated on the basis of images of quartz capillaries (0.3 – 4 mm diameters) filled with nanodiamond suspensions with repositioning on anatomical images obtained via X-ray micro-computed (micro-CT) tomography.

*Image reconstruction and mathematical procedures.*

EPR image reconstruction were performed using a Total Variation algorithm-based [41], published and usable online [42].

*X-ray microtomographs.* Micro-CT imaging was performed using a 1178 X-ray computed scanner (Skyscan, Kontich, Belgium) with the following parameters setting: 65 kV, 615 µA, pixel size 83.82932 µm. Spatial resolution of quartz capillary diameters was determined by analyzing the micro-CT images using the Skyscan software suite. The images were co-registered using GIMP®.

## Results and discussion

### Physicochemical characterization of NDs (as-received $ND_{DET}$ and $ND_{HPHT}$)

For $ND_{HPHT}$, we used as-received (asrec) commercially available MSY 0 – 0.03 as these are the smallest monocrystalline particles reported [43]. TEM analysis revealed NDs with irregular shapes with sharp edges and a large size distribution (17 nm, $PDI^{TEM}$: 1.79). The particle size

distributions obtained after sonication show narrow, almost monodisperse particle distributions (24 nm in number-weighted distributions) (**Fig. 1a**), consistent with TEM observations. For $ND_{DET}$, while small-sized particles were observed by TEM (5.2 nm, $PDI^{TEM}$: 1.44), a larger average particle size was observed using DLS (63 nm and 32 nm in intensity- and number-weighted distributions, respectively), suggesting the dispersion of aggregates rather than individual particles. On the contrary to $ND_{HPHT}^{asrec}$, $ND_{DET}^{asrec}$ were characterized by low colloidal stability ($\zeta$ = - 39 and + 42 mV, pH 7.3), respectively, especially when the ionic strength of the medium is increased, which could reflect significant differences in their surface chemical composition. IR analysis confirmed this hypothesis by revealing a characteristic band at 1766 $cm^{-1}$, corresponding to the C=O stretching of carboxylic acid groups, present only on $ND_{HPHT}^{asrec}$ (**Fig. S2b**). This feature is responsible for the negative zeta potential that ensures their colloidal stability. On both types, additional signatures of oxidized terminations, such as alcohols and epoxy groups, are indicated by bands at 1290 $cm^{-1}$ and 1090 $cm^{-1}$, corresponding to symmetric and asymmetric C-O stretching modes, respectively. Bands at 3670 – 2670 $cm^{-1}$ and 1620 $cm^{-1}$, associated with O-H stretching and bending modes respectively, are also observable. These may originate from alcohol functions or from adsorbed water on the ND surface. Finally, $ND_{DET}^{asrec}$ shows a structure between 2800 and 2950 $cm^{-1}$, corresponding to aliphatic C-H stretching modes due to hydrogen terminations and/or non-diamond phases on the surface.

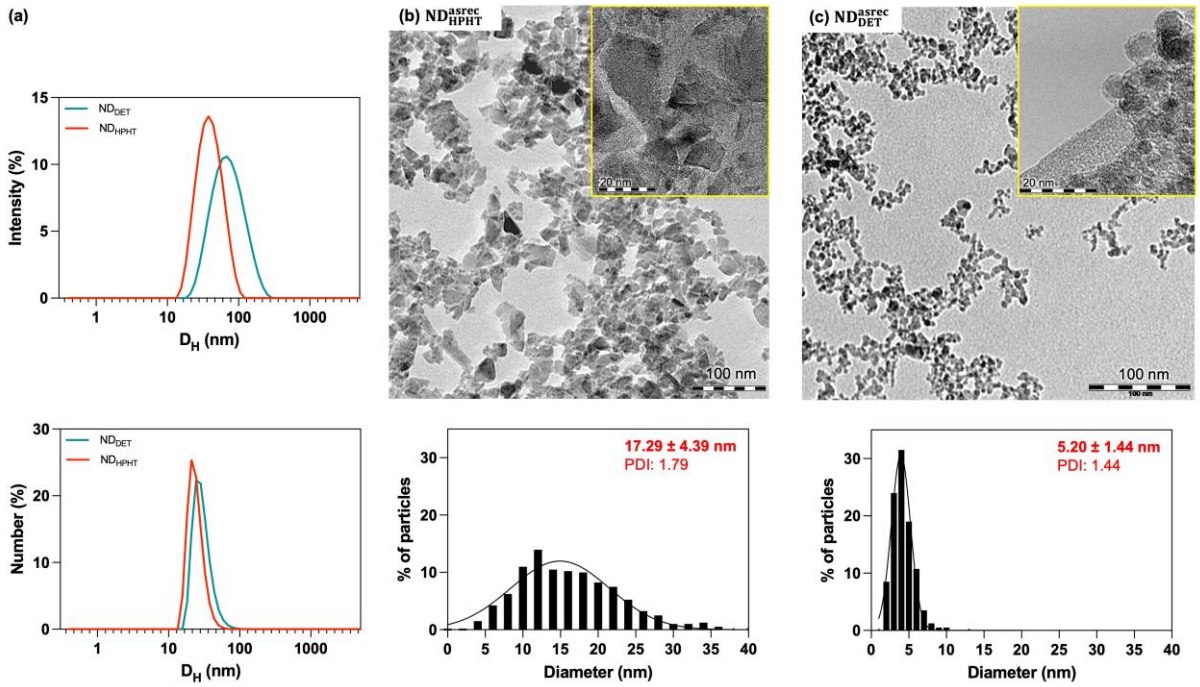


**Figure 1. Size measurements. (a)** Size distributions obtained by PCS (intensity-weighted, (up) and number-weighted (bottom) distributions. TEM images of **(b)** mean 17 nm $ND_{HPHT}$ and **(c)**

mean 5 nm $ND_{DET}$ (scale bars: 100 nm) and their particle size distributions. The x axis for $ND_{HPHT}$ particle histograms is expressed as a 2-nm increment size diameter for clarity (1-nm increment size for $ND_{DET}$). Extensions (yellow frames) show high-resolution TEM images (scale bars: 20 nm) obtained by HRTEM-EDX experiment (as-received HPHT and detonation samples: 200 k and 250 k × magnification, respectively).

Using high-frequency (X-band, 9 GHz) EPR acquisitions, we can assess that both samples $ND_{HPHT}$ and $ND_{DET}$ (10 mg $mL^{-1}$) contain electron spins with a main spectroscopic splitting factor (*g*-factor) = $g_e$ = 2.0027 ± 0.0002. Among impurities other than carbon, some paramagnetic and ferromagnetic impurities originating from transition metal ions ($Fe^{3+}$, $Cr^{3+}$, $Mn^{2+}$, $Co^{2+}$, $Ni^{2+}$ or $Cu^{2+}$) can be found in diamond suspensions. HR-TEM energy-dispersive X-ray (EDX) have confirmed the presence of Al, Fe or Zr (**Table S1**) randomly distributed within the bulk, among others elements, with uniform distribution [39,44]. As a result of the grinding and explosion processes (milling with zirconium oxide micron-sized beads, sonic mechanical disintegration of corrosion products from the explosion chamber wall) non-carbon elements were incorporated within suspension. ICP-AES analysis estimated the bulk composition of $ND_{DET}^{asrec}$ and $ND_{HPHT}^{asrec}$ suspensions. The resulting concentrations normalized per NDs suspension are listed in **Table S2**. Among the most notable differences between both samples, one has to mention the high zirconium content detected in $ND_{DET}$ sample (with around 14 ng per mg $ND_{DET}$ and below LOD in $ND_{HPHT}$ sample) as a consequence of their dispersion process ($ND_{DET}$ dispersion is achieved using zirconia beads-assisted method).

**Figure 2** shows the main resonance EPR single lines at 343 mT (extension) for $ND_{HPHT}$ and $ND_{DET}$ samples, resulting mainly from structural defects (dangling bonds). For small-sized nanodiamonds (< 70 nm), it can be assumed as a two component deconvolution, since the EPR line has a larger linewidth, with a similar signal resonance *g*-factor, mainly attributed to the free electron resonance ($g_e$ = 2.0027) but with different linewidth contributions [45]: (i) a broad spin-½ Lorentzian component assigned to C-C carbon dangling bonds on the particle surface and in the nanoparticle core, and (ii) a narrow spin-½ Lorentzian component attributed to defects in the diamond lattice [45]. Due to the relatively high local spins densities and their close proximity, a main characteristic of a nanosized system, these defects are able to mutually interact, and additionally, can interact with nearby P1 centers, increasing the linewidth. Here, the main differences between nanodiamonds are the production origin, crystallographic core, internal/surface defects, purification, surface chemistry, agglomeration state, presence of $sp^2$-carbon and

the material size. The experimental resonance measured on the $ND_{DET}^{asrec}$ and $ND_{HPHT}^{asrec}$ was characterized by peak-to-peak linewidths of 0.96 mT and 0.38 mT, respectively, at a resonance field $B_0$ ~ 343.5 mT. In order to understand the surface etching modification, nanodiamond source, or size effect, we compared the EPR signal peak-to-peak linewidth (lwpp). It is worth noting that similar 18 nm-$ND^{HPHT}$ particles from a different provider have been previously reported [46], with a focus on particles of similar size and characteristics.

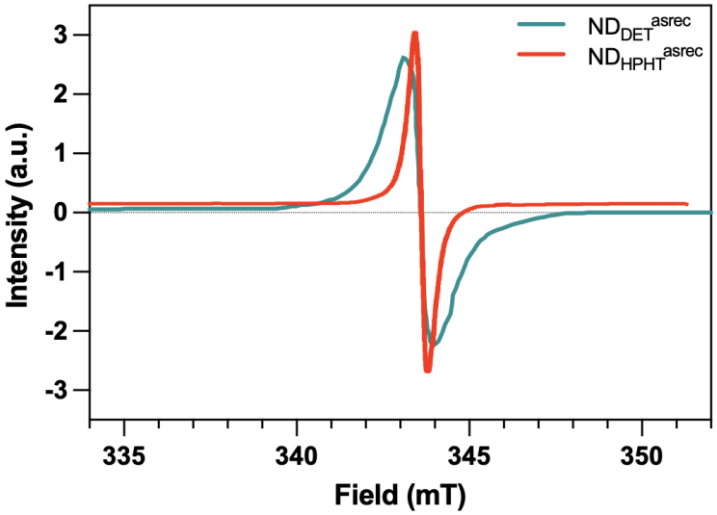


**Figure 2.** Typical analysis of high-frequency (X-band) EPR profiles of $ND_{DET}^{asrec}$ (green) and $ND_{HPHT}^{asrec}$ (red) suspensions (10 mg $mL^{-1}$) recorded at room temperature (main resonance signal) around the resonant magnetic field of the signal ($g$ = 2.0027). Microwave frequency: 9 GHz.

**Physicochemical modifications of NDs**

*Air oxidation process*

$ND_{DET}$ have a complex surface nature with a higher density of surface defects, amorphous and graphitic carbons and a wide diversity of functional groups, which can be modulated by surface oxidation to generate acid functions. Oxidation by air-annealing provides an efficient method for oxidizing ND surface and removing non-diamond carbon, including paramagnetic radical-like centers (*i.e*. dangling bonds) [34]. *Prior* to this, thermogravimetric analysis (TGA) were performed on these materials to evaluate their thermal behavior applying a heating rate of 10°C/min (**Fig. S1a**); $ND_{DET}$ and $ND_{HPHT}$ begin to decompose at 515 and 483°C, respectively, with a weigh loss of 5%. A weight loss of 50% is observed between 546 and 560°C, respectively. Based on information resulting from TGA analysis, air-annealing conditions at 400°C

(ox-1), 450°C (ox-2), 480°C (ox-3) or 550°C (ox-4) for 4 hours were applied in order to evaluate the impact of oxidation on ND physicochemical properties, especially with regard to their surface chemical composition, graphitization or dangling bonds onto ND surface. Thanks to the annealing process, the weight decreases to 96 or 87% at 400°C, 90 or 86% at 450°C, 84 or 68% at 480°C and to 31 or 1% at 550°C after 4 hours of air-annealing for $ND_{HPHT}$ and $ND_{DET}$, respectively (**Fig. S2**).

In $ND_{DET}$ samples, primary particles appear as tightly bounded clusters, forming large aggregates in suspension as a result of their surface nature due to various functional groups (*i.e.* ether, epoxide, hydroxyl, carbonyl, carboxyl). The first observation is that the applied treatments improve the dispersion as well as the colloidal stability by preventing NDs from aggregation. This observation is confirmed by PCS analyses. While no significant difference in the core size was noted by TEM (5.2 ± 1.4 nm *vs.* 4.5 ± 1.2 nm), PCS indicates that this treatment has a considerable decrease in the mean hydrodynamic size from 63 nm ($D_{\#}^{PCS}$ = 28 nm) for $ND_{DET}^{asrec}$ to 45 – 48 nm ($D_{\#}^{PCS}$ = 15 – 22 nm) for oxidized $ND_{DET}$ samples, respectively. The evolution of zeta potential in relation to pH changes indicates a shift from positive to negative values (from $\zeta$ = + 46 mV to - 44 mV after oxidation, at pH 7.3; **Fig. S3**), suggesting an increase of colloidal stability through ionic repulsion. Indeed, FT-IR analysis reveals the emergence of a carbonyl C=O stretching band around 1780 $cm^{-1}$, indicating the formation of carboxylic groups on the surface. This is responsible for the negative zeta potential, in concomitance with the disappearance of C-H stretching modes previously observed. **Figure S4** also shows that the annealing at 400°C leads to a similar spectrum to those obtained under other conditions (up to 500°C). In accordance with FT-IR, XPS data (**Fig. S5**) showed an increase in the total oxygen content in the $ND_{DET}^{ox-1}$sample after air-annealing (**Table S3**); their atomic concentrations were calculated from the corresponding *C1s* and *O1s* core levels peak intensities (286 – 280 eV and 531 – 528 eV ranges, respectively). The main difference in elemental composition in relative percentage terms is expressed by the *O1s/C1s* ratio. While $ND_{DET}^{asrec}$ nanodiamonds contain 3.80% oxygen and 94.20% carbon (the remaining 2% consists of nitrogen) (*O1s/C1s* = 0.04), $ND_{DET}^{ox-1}$ contain 9.41% oxygen and 89.19% carbon (*O1s/C1s* = 0.10). This corresponds to a 59% increase in oxygen and a 5% reduction in carbon after air-annealing under ox-1 conditions. Following the air-annealing treatment, the surface composition of $ND_{HPHT}$ seems to be less affected as suggested by the slight evolution observed in the various FT-IR spectra (**Fig. S4**). This observation suggests that, unlike $ND_{DET}^{asrec}$, $ND_{HPHT}^{asrec}$ surface was already completely oxidized due to the grinding process nature [47]. XPS (**Figure 3)** confirms those observations with no significant

difference observed for $ND_{HPHT}$ samples under the same air-annealing procedure (*O1s/C1s* = 0.11). After their US-assisted dispersion in DI water, PCS measurements indicate that controlled air-annealing at 400°C, 450°C, 480 or 550°C for 4 hours compared to $ND_{HPHT}^{asrec}$ procedure has no influence on their colloidal behavior based on their hydrodynamic particle size distribution profiles (around $D_H^{PCS}$ 36 nm) and zeta potential values (around $\zeta$ = - 45 mV at pH 7.4). Overall, the quantitative analysis of the evolution of the carboxylic acid content in $ND_{DET}$ samples indicated an increase of 19 to 27 nmol $mg^{-1}$ between $ND_{DET}^{asrec}$ and $ND_{DET}^{ox-1}$ conditions, as determined by Boehm conductimetric titration. In the case of $ND_{HPHT}$, no significant difference was noticed in these conditions (32 nmol $mg^{-1}$). This average amount corresponds to 0.36 COOH groups per $nm^2$ of spherical $ND_{DET}^{ox-1}$ particle surface.

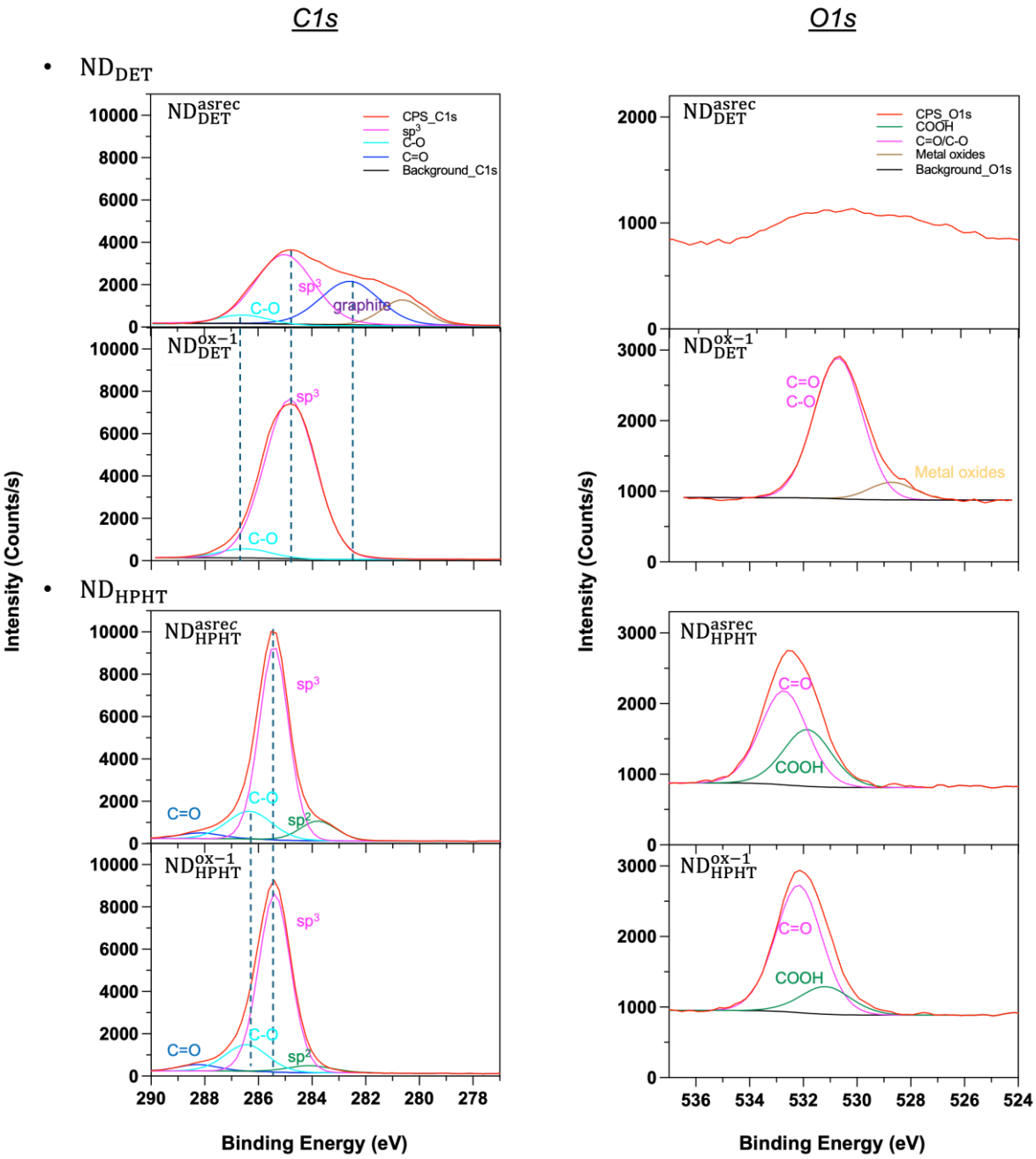


**Figure 3. XPS data.** Deconvoluted and experimental *C1s* and *O1s* fits of $ND_{DET}$ and $ND_{HPHT}$ **(columns)** obtained before and after air-annealing for 4 h. Highlighted *C1s* and *O1s* data can be found in **Table S3**.

*Size exclusion process*

Due to the polydispersity of $ND_{HPHT}$, we use a simple size exclusion approach to reduce the particle size distribution, and approximate the distribution obtained for $ND_{DET}$ after thermal

treatment. Size sorting process using centrifugation is a common and simple approach to satisfying colloid fractionation [35,36]. Previous reports showed that MSY 0 – 0.05 (25 nm median size) are composed of 59% (based in number-weight distribution) of NPs smaller than 17 nm, in particular, 33% of 5 nm $ND_{HPHT}$, as revealed by TEM analysis [36]. Herein, the high polydispersity (1.79) of the $ND_{HPHT}^{asrec}$ material offers the obvious advantage of being able to be separable into distinct subdivision fractions starting from the crude $ND_{HPHT}^{asrec}$ (0.5%$_{wt./v}$). We assumed a similar distribution in the MSY 0 – 0.03 sample. To roughly evaluate the size distribution influenced by centrifugation, we employed a constant high-speed (16,800 g) with extended durations in 60-minutes increments to generate a series of sub-17 nm fractions. After each centrifugation cycle, the supernatant was carefully separated to isolate the $ND_{HPHT}$ sub-17 fractions. By following this procedure, we were able to systematically reduce the size of the $ND_{HPHT}$ sample; substantial differences were observed between the recorded distributions, indicating a shift towards smaller particle diameters, as confirmed by PCS measurements (**Fig. 4**). Starting from the initial $ND_{HPHT}^{asrec}$ material ($D_{\#}^{PCS}$: 24.2 nm; PDI: 0.188), the number size profiles clearly show a significant reduction in size distribution well below $D_{\#}^{PCS}$ 13.2 nm (PDI: 0.164) after the first treatment cycle (1 × 60 min; $ND_{HPHT}^{1}$ sample).

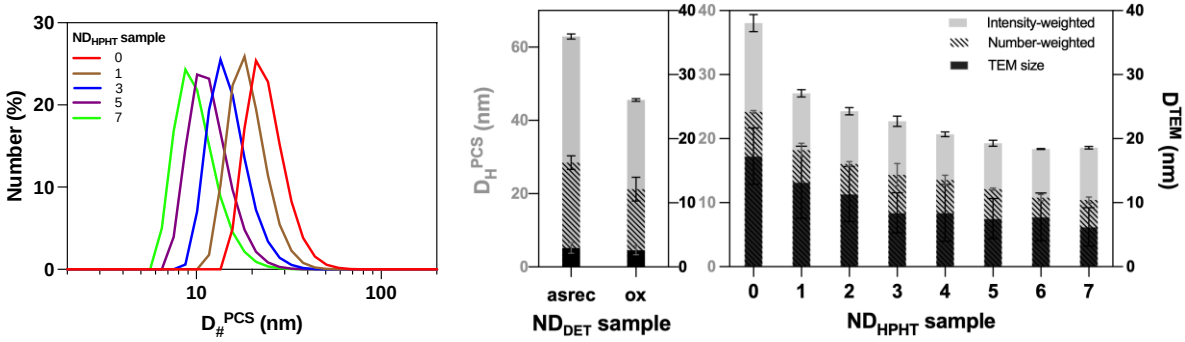


**(a)** **(b)**

**Figure 4. Size distributions. (a)** Number size distributions obtained by size exclusion, starting from raw $ND_{HPHT}^{asrec}$. Only $ND_{HPHT}$ fragments isolated after 1, 3, 5 and 7 cycles (16,800 g) of 60-min of increment are shown for clarity. **(b)** Size distributions histograms by intensity- and number-weighted and TEM sizes ± standard deviations plotted as function of the number of cycles ($ND_{HPHT}^{asrec}$ is written as "0", $ND_{HPHT}^{1}$ referred "1", etc) and comparison to $ND_{DET}$ colloids. Note that the y axis ($D_{\#}^{PCS}$) for $ND_{DET}$ and $ND_{HPHT}$ samples is adjusted between nanodiamond sample type for clarity.

Efficient size exclusion was observed from the third centrifugal treatment ($ND^{3}_{HPHT}$ sample; $D_{\#}^{PCS}$: 14.3 nm (PDI: 0.132)). In correlation with DLS, TEM analysis confirmed the PCS observations, showing an evolution of the mean size from 17.3 ± 4.4 nm (PDI: 1.79) to 8.4 ± 3.1 nm (PDI: 1.54) (**Fig. 5**) for raw to $ND^{3}_{HPHT}$ (37% in particle concentration) respectively, as depicted in the proposed sorting process. The particle size of sub-17 nm HPHT thus approached that obtained for detonation particles. No significant difference in the size profile could be noticed between $ND^{3}_{HPHT}$ compared to the other sub-fractions. Overall, this size treatment effectively isolated the desired sub-17 nm particles, resulting in a relatively monodisperse fraction (**Table S4**), despite a relatively low yield (around 7.5%$_{wt.}$ in particle concentration), based on the initial colloid concentration, as obtained gravimetrically (**Fig. S6, Table S4**).

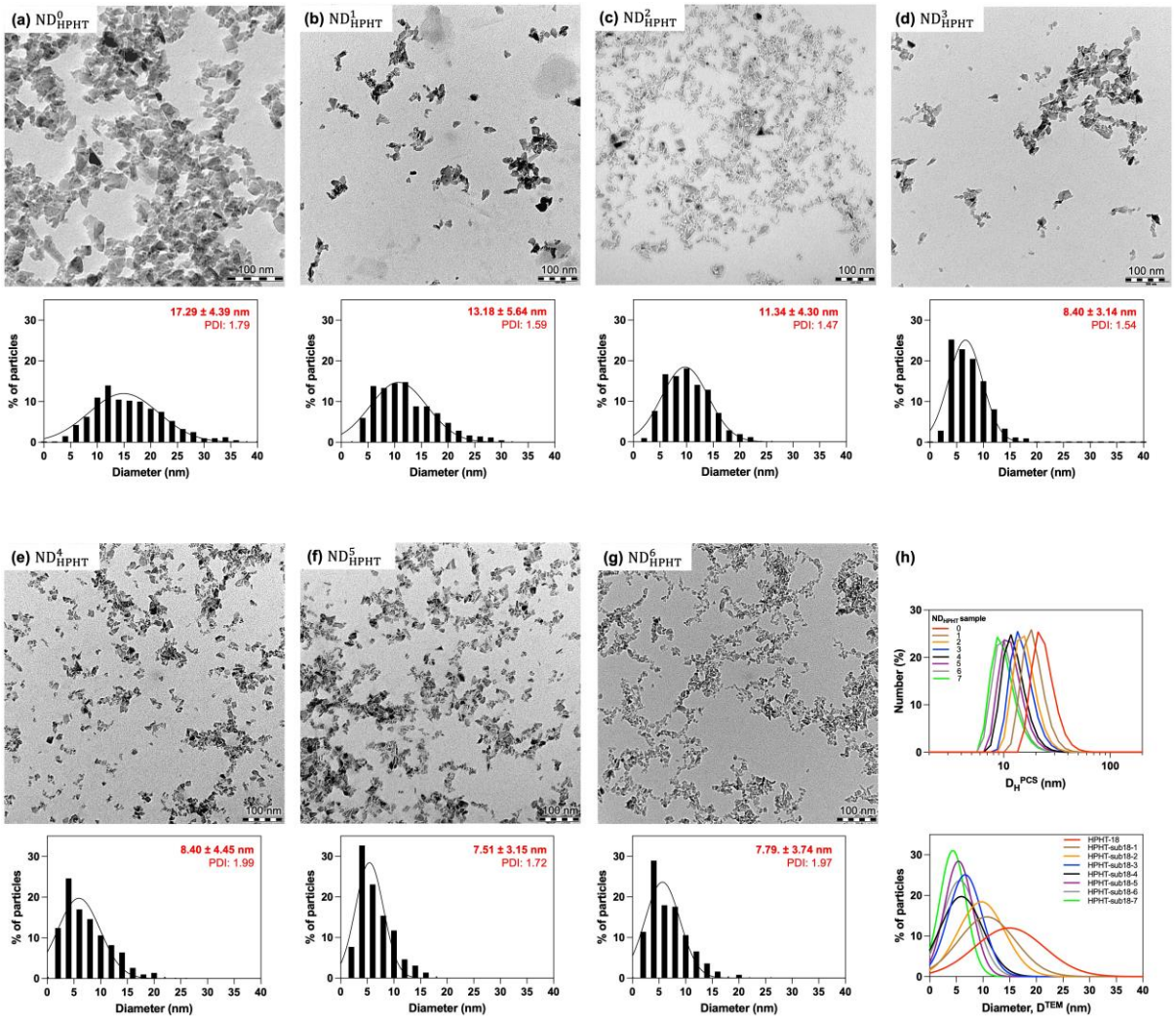


**Figure 5. Size measurements on $ND_{HPHT}$ size exclusion particles.** TEM images from **(a)** to **(g)** (scale bars: 100 nm) and statistical analysis after centrifugation with 60-minutes of increment starting from $ND^{asrec}_{HPHT}$ sample (core size approxim. 18 nm). The histogram diameter axis

is set by 2-nm increment for clarity. **(h)** Dynamic size distributions (number-weighted distributions) of the isolated $ND_{HPHT}^{sub-17}$ fractions following centrifugation treatment at 16,800 g, starting from $ND_{HPHT}^{asrec}$ (0 min) showing a shift towards smaller $D_{\#}^{PCS}$ distributions (up). Comparison of TEM size distributions using histograms fitted with a log-normal function (down).

It must be mentioned that the separation of detonation nanoparticle was not a straightforward applicable process; indeed, 16,800 g speed treatment led to a non-stable suspension due to their aggregation states caused by the complex structure of the isolated detonation shoot. Photos of as-received and thermally oxidized particles treated for 60-min at 16,800 g are shown in **Figure S7.** This procedure was not applied to the detonation nanodiamonds due to a lack of colloidal stability resulting from their aggregation state. We note that these particles are usually tightly bound into aggregates, despite many efforts (milling aggregates with micrometer-sized ceramic beads) to stabilize individual spherical NP [48].

**EPR spectroscopic and imaging study for spatial resolution**

***HPHT-synthesized nanodiamonds***

Interestingly, a noticeable linewidth reduction effect can be observed in EPR spectroscopy from 0.38 mT onwards as the average particle size decreases through size exclusion. The EPR features (signal width) of this series of HPHT are presented in **Table 1**. The linewidth decreased and then reached a plateau from sample $ND_{HPHT}^{3}$ to $ND_{HPHT}^{5}$ ($ND_{HPHT}^{3}$; $N_s$ = 1.3 $10^{19}$ spin/g) for a value of around 0.23 mT, corresponding to a decrease in the broad component of nearly 40%, for which $ND_{HPHT}^{3}$ sample appeared as an efficient sample for EPRI investigation (achievable resolution < 0.5 nm). This set of size variations $ND_{HPHT}$ resulted in a weak decrease of spins per g ($N_S$), however, strikingly, an efficient decrease in the broad component of the signal. The comparison of physicochemical parameters collected for the different series of nanodiamonds is summarized in **Table 1**.

**Table 1.** Comparison of physicochemical parameters of nanodiamonds.

| | | **Size** | | **EPR (X-band)** *(g = 2.0027 ± 0.0002)* | | **EPRI** |
|---|---|---|---|---|---|---|
| **Sample** | **ζ** pH=7.3±0.1 (mV) | **$D_{\#}^{PCS}$** Num.-w (nm) | **$D_H^{PCS}$** Int.-w (nm) | **lwpp** (mT) | ***$N_S$*** (spin/g) | ***R*** (mm) |

| | | | | | | |
|---|---|---|---|---|---|---|
| $ND_{DET}^{asrec}$ | + 42 ± 2 | 28.4 ± 1.9 | 62.9 ± 0.7 | 0.96 | 6.6 $10^{19}$ | >2 |
| $ND_{DET}^{ox-1}$ | - 40 ± 2 | 21.2 ± 3.2 | 45.6 ± 0.4 | 0.88 | 5.8 $10^{19}$ | >2 |
| $ND_{HPHT}^{asrec}$ | - 39 ± 2 | 24.2 ± 0.2 | 36.1 ± 0.2 | 0.38 | 1.5 $10^{19}$ | 0.7 |
| $ND_{HPHT}^{1}$ | - 37 ± 2 | 27.1 ± 0.6 | 27.1 ± 0.6 | 0.27 | 1.4 $10^{19}$ | >0.5 |
| $ND_{HPHT}^{3}$ | - 36 ± 1 | 14.3 ± 1.8 | 23.9 ± 0.3 | 0.23 | 1.3 $10^{19}$ | 0.5 |
| $ND_{HPHT}^{5}$ | - 44 ± 2 | 12.2 ± 0.2 | 19.3 ± 0.4 | 0.23 | 1.0 $10^{19}$ | <0.5 |
| $ND_{HPHT}^{7}$ | - 44 ± 2 | 10.4 ± 0.5 | 18.6 ± 0.2 | 0.22 | 9.8 $10^{18}$ | <0.5 |
| $ND_{HPHT}^{ox-1}$ | - 43 ± 1 | 22.6 ± 0.6 | 35.4 ± 0.1 | 0.28 | 1.6 $10^{19}$ | >0.5 |
| $ND_{HPHT}^{ox-2}$ | - 46 ± 1 | 21.2 ± 0.8 | 34.5 ± 0.2 | 0.27 | 9.1 $10^{18}$ | >0.5 |
| $ND_{HPHT}^{ox-3}$ | - 46 ± 1 | 21.0 ± 1.2 | 37.8 ± 0.1 | 0.26 | 6.7 $10^{18}$ | 0.5 |
| $ND_{HPHT}^{ox-4}$ | - 47 ± 1 | 15.6 ± 1.1 | 32.6 ± 0.5 | 0.24 | 2.1 $10^{18}$ | <0.5 |

Alternatively, thermal annealing of $ND_{HPHT}$ resulted in a decrease in the broad component of the signal. In contrast to detonation nanodiamonds, the air-annealing process has minimal impact on the spins located on the outer surface due to the surface nature of HPHT particles.

Although FTIR spectroscopy did not reveal any significant qualitative differences between the samples after thermal treatments, there was a significant impact on their lwpp. Raman spectroscopy was used to determine these differences. This technique provided additional information on their structural changes. The Raman spectrum of $ND_{HPHT}$ is shown in **Fig. S8a** and displays the following characteristics [49]: (i) a peak at 1330 $cm^{-1}$ (dotted line) associated with the first order diamond peak (C*, diamond phase); (ii) the deconvoluted peak at 1350 $cm^{-1}$ is assigned to $sp^2$-hybridized bonds deformation mode (D-band); (iii) 1470 $cm^{-1}$ could be attributed to the presence of nitrogen-vacancy defects in the diamond lattice; (iv) a broad component at 1570 – 1590 $cm^{-1}$ due to allotropic forms of carbon $sp^2$-graphitic carbon covering the diamond core (G-band); (v) a band at 1685 $cm^{-1}$ characteristic of C-OH / C=O bending vibrations at particle surface. Within addition to the above-mentioned peaks, the $ND_{HPHT}$ 1580 $cm^{-1}$ peak (G-band) decreases due to air-annealing progress of HPHT samples (400 to 550°C) among the others non-diamond absorption (**Fig. S8a**). Indeed, Raman spectra of HPHT particles show a considerable increase in the diamond peak (C*) intensity compared to the broad $sp^2$-related band (1500 – 1800 $cm^{-1}$) of the air-annealed samples and its shift 1332 – 1333 $cm^{-1}$ becomes dominant (**Fig. S8b)**. It is evident that the air-annealing of HPHT powder at 550°C for 4 hours ($ND_{HPHT}^{ox-4}$) considerably reduces the graphitic content as the G-band is further suppressed.

For both strategies, these distinct treatments enabled adequate control of size and surface area, leading to a fine tuning of parameters and lower $N_S$ content. Overall, the EPR signal of HPHT particles typically exhibits a narrower linewidth for the narrow component, compared to other types of nanodiamonds. This suggests a higher degree of order in the material, although linewidths are also influenced by other factors, such as the initial content of P1 centers and exchange interactions between spins within the particle [45]. This is particularly true as the size decreases from micrometers (100 µm) to nanometers (20 nm) as reported in the literature [50]. Distinctive modifications (including signal linewidth) have appeared in the EPR spectrum when the average size of particles in polydisperse samples decreases [50].

***DET nanodiamonds***

In contrast, the EPR signal of detonation nanodiamonds typically exhibits a broad linewidth (lwpp = 0.96 mT) due to the presence of multiple paramagnetic defects such as structural defects, dangling bonds, impurities, graphite and diamond allotropes [51]. Overall, HPHT nanodiamonds exhibit a narrower signal than $ND_{DET}^{asrec}$, representing a reduction of almost 60% of the FWHM (full width at half maximum). In addition, the concentration of RPC (spin $S$ = ½) was estimated to $N_s$ = 1.5 $10^{19}$ spin/g on the HPHT colloid which is ~ 4.4 times less than detonation sample ($N_s$ = 6.6 $10^{19}$ spin/g). Assuming that $ND_{DET}^{asrec}$ particles are spherical, an experimental value of approximately 5 RPC/particle is obtained, and the spins are inhomogeneously distributed according to literature [48,51]. Interestingly, we observe a reduction in the EPR signal linewidth resulting from the decrease in spin density at the particle surface during air-oxidation treatment. For comparison, oxidative treatment of $ND_{DET}$ reduces the broad component by 10% associated with impurities near the particle surface (mainly dangling bonds) for ox-1 sample. This fact illustrates the importance of surface properties and sets for surface development.

The main advantage of $ND_{HPHT}$ over $ND_{DET}$ is the uniform crystallinity and purity with a relatively low and localized concentration of spin resonant lattice defects. This is crucial for their spectroscopic characteristics and imaging applications, as they can stably host narrow single line EPR components. The concentration of radical-like paramagnetic centers, including impurities and dangling-bonds, can be well-suited to EPRI applications with significant decreases in peak-to-peak derived linewidth after $ND_{HPHT}$ size exclusion. Three centrifugation cycles of the $ND_{HPHT}$ nanodiamonds yield to promising EPR features (minimal lwpp obtained = 0.22 mT). In an interesting feature involving nanodiamonds, we highlight how the use of NDs can be

relevant to afford a unique EPR contrast signature through long-term stable paramagnetic centers.

**L-band EPR imaging study for spatial resolution**

Imaging capabilities of NDs have been further evaluated in L-band (1 GHz) EPR spectroscopy (**Fig. S9**) and imaging for low-field frequency measurements. EPR images are recorded similarly as a conventional EPR spectrum, with magnetic field gradients applied in a range of different orientations around the sample (gradient = 4 mT/cm). The achievable resolution in an EPRI experiment is based on concepts similar to those of MRI acquisition. Formally, a common definition of resolution is the determination of the number of pixels in a specified field of view (FOV). In this case, the theoretical spatial resolution in EPRI is closely proportional to the peak-to-peak linewidth of the EPR spectroscopic absorption curve (lwpp) and the inverse of the gradient intensity ($\nabla$), typically, $R = lwpp/\nabla$. Overall, a narrower linewidth and stronger gradients allow for high resolution EPR images ($\lim_{\nabla \to \infty} R = 0$), which is limited by the magnetic field produced by the gradients [52] for small gradient strength ($\nabla$ < 10% principal magnetic field). Two-dimensional imaging also implies spatial resolution represented by the pixel resolution ($R_{Pixel} = FOV/Number\ of\ Pixel$) of the imaging system with correct image reconstruction [41]. However, broad peak-to-peak linewidths can limit the application of various types of NPs for resolution enhanced imaging, which tends to give special attention to nanometric $ND_{HPHT}$. In this case, employing a deconvolution process to recover a spatially homogeneous spin density distribution, spatial resolutions of less than 0.7 mm could be obtained in the improved EPR imaging system starting from the raw $ND_{HPHT}^{asrec}$ sample. Using mathematical algorithms and imaging optimizations, we present promising preliminary EPRI acquisitions of capillary phantoms after image reconstruction. The experimental resolution of $ND_{HPHT}^{asrec}$ was evaluated by image analysis based on quartz capillaries containing mean 18 nm size monocrystalline particles with inner-diameter sizes ranging from 0.2, 0.3, 0.4, 0.5, 0.6, 1 and 4.0 mm. Imaging of raw $ND_{HPHT}^{asrec}$ (lwpp = 0.38 mT; RPC = 0.442 mM) filled into capillaries at a similar concentration (10 mg $mL^{-1}$) showed a strong detectable signal. An achievable resolution of < 0.7 mm was observed on **Figure 6** with spatial registration and fusion of raw EPRI and X-ray micro-CT on the same object. In contrast, $ND_{DET}$ (lwpp = 0.98 mT) did not provide the expected resolution since $R$ > 2 mm under the data acquisitions ($R$ = 0.23 mm for a FOV of 32 mm) (data not shown). We can mention that $ND_{DET}$ EPR signal operating at microwave frequency of 1 GHz presents a known spectral resolution limitation compared to $ND_{HPHT}$ sample. Despite a 4.4-fold decrease in RPC

content compared with $ND_{DET}$, typically exhibiting a spin density $N_S$ of 6.6 $10^{19}$ spin/g versus 1.5 $10^{19}$ spin/g, for $ND_{DET}^{asrec}$ and $ND_{HPHT}^{asrec}$, respectively, the latter still demonstrates good sensitivity and threshold detection.

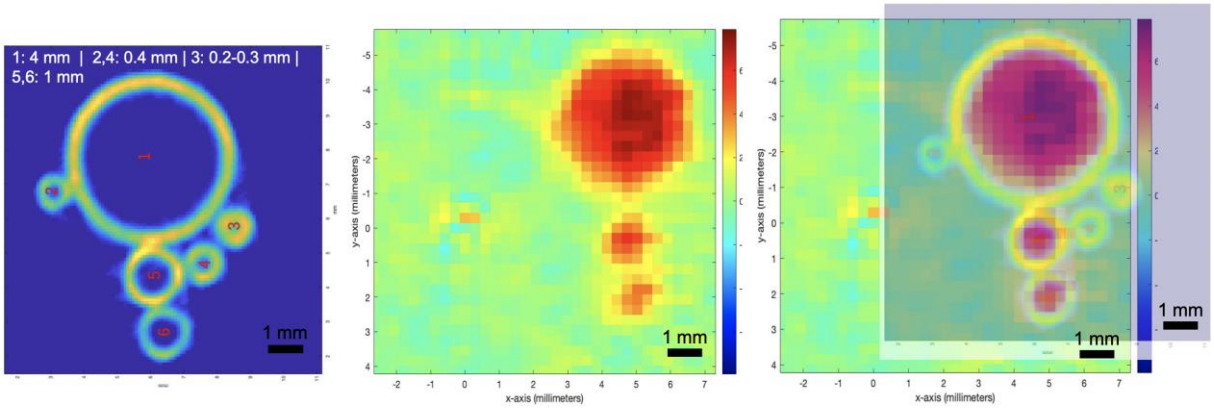


**Figure 6. L-band EPR imaging experiment of $ND_{HPHT}^{asrec}$ sample.** Anatomic Micro-CT image (left), corresponding 2D image (ZY) of glass capillaries containing NDs suspensions imaged by EPRI (middle) and the superimposed spatial registration of the EPR image to the corresponding micro-CT scan (right). EPRI parameters: experimental time: 71 min; lwpp: 0.35 mT; FOV: 37.55 mm.

Additionally, as previously mentioned, the spatial resolution of EPR images (*R*) depends on probe linewidths and the magnetic field strength. Thus, reducing the linewidth of the sample may enhance image contrast. From all the samples under study, we consider $ND_{HPHT}^{3}$ colloid to be the most promising (lwpp = 0.23 mT). Furthermore, if the number of spins in a pixel or voxel falls below the detection threshold (< 0.4 mm), no image can be acquired under these conditions. On this basis, we investigate nanodiamonds density of $ND_{HPHT}^{3}$ sample studying a 10 mg $mL^{-1}$ (RPC = 0.221 mM) (**Fig. 7**; upper line) or 20 mg $mL^{-1}$ (RPC = 0.442 mM) (**Fig. 7**; lower line) suspension. Full details specific to sampling imaging parameters can be found in the paper from Abergel *et al*. [42]. Images were processed according to the number of iterations.

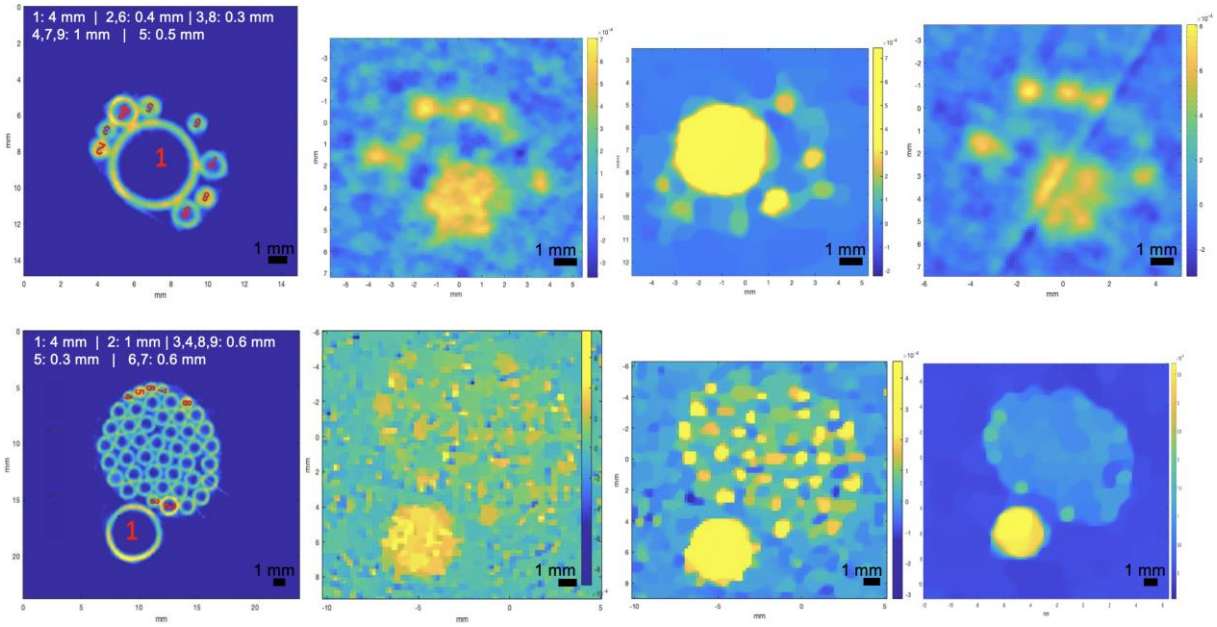


**Figure 7. L-band EPR images of $ND^{3}_{HPHT}$ sample.** EPRI and the phantom object anatomic CT-microtomography (left) and 2D images (ZY) of glass capillaries containing aqueous suspensions of NDs from left to right according to iteration number, regularity parameter λ′. ND densities of 10 mg $mL^{-1}$ (up) and 20 mg $mL^{-1}$ (down) were imaged.

The images above represent the first combined EPRI and micro-CT images offering good resolution of a phantom ($R$ < 0.5 mm) and open the way to the utilization of NDs in the field of EPR imaging.

## Conclusion

This study explores the physicochemical properties of nanodiamonds, focusing on size and surface treatments using commercial materials obtained by grinding or detonation synthesis. The difference in production conditions allows to differ the chemical composition of impurities and their distribution along the crystal as well as a control over a predetermined nanoparticle size and shape. Using size exclusion on a polydisperse HPHT sample (mean size 18 nm), a particle size distribution similar to that of detonation nanodiamonds was achieved, with improved structural quality and surface uniformity. In addition, we describe thermal oxidation because it is a straightforward approach that allows surface chemistry uniformization leading to oxygen-terminated particles and compared EPR features. Furthermore, EPR spectroscopy revealed the promising properties of HPHT nanodiamonds for probing at smaller sizes, demonstrating the capabilities of low-field (1 GHz) EPR imaging. Overall, this study highlights the unique EPR

properties of nanodiamonds, specifically $ND^{3}_{HPHT}$ sample (mean size of 8 nm) and offers prospects for applications in nanomedicine and materials science.

## Associated content

The Supporting Information is available.

HRTEM-EDX data (Table S1), ICP data (Table S2), XPS data (Table S3), size data (Table S4). Surface analysis (Figure S1), gravimetric measurement (Figure S2), zeta potential data (Figure S3), IR (Figure S4), XPS spectra (Figure S4), size obtained by size exclusion (Figure S6), photographs of ND suspensions through size exclusion process (Figure S7), Raman spectra (Figure S8) and L-band EPR spectrum of ND sample (Figure S9).

## Author information


### Corresponding author

Sophie Laurent – (1) NMR and Molecular Imaging Laboratory, General, Organic and Biomedical Chemistry Unit, University of Mons, B-7000 Mons, Belgium. (2) Center for Microscopy and Molecular Imaging (CMMI), B-6041 Gosselies, Belgium. https://orcid.org/0000-0002-2589-3250

E-mail: sophie.laurent@umons.ac.be; Tel.: +32-65373594

### Authors

Sarah Garifo – NMR and Molecular Imaging Laboratory, General, Organic and Biomedical Chemistry Unit, University of Mons, B-7000 Mons, Belgium. https://orcid.org/0000-0003-1137-7690

Dimitri Stanicki – NMR and Molecular Imaging Laboratory, General, Organic and Biomedical Chemistry Unit, University of Mons, B-7000 Mons, Belgium. https://orcid.org/0000-0002-6530-9901

Thomas Vangijzegem – NMR and Molecular Imaging Laboratory, General, Organic and Biomedical Chemistry Unit, University of Mons, B-7000 Mons, Belgium. https://orcid.org/0000-0001-5695-9307

Philippe Mellet – (1) University of Bordeaux, CNRS, CRMSB, UMR 5536, F-33000 Bordeaux, France. (2) INSERM, F-33000 Bordeaux, France. https://orcid.org/0000-0001-5499-9735

Hugues A. Girard – Université Paris-Saclay, CEA, CNRS, NIMBE, 91191 Gif sur Yvette, France. https://orcid.org/0000-0001-8491-0412

Jean-Charles Arnault – Université Paris-Saclay, CEA, CNRS, NIMBE, 91191 Gif sur Yvette, France. https://orcid.org/0000-0002-1081-3449

Sylvie Bégin-Colin - UMR CNRS-UdS 7504, Institut de Physique et Chimie des Matériaux, CNRS, University of Strasbourg, 67034 Strasbourg, France. https://orcid.org/0000-0002-2293-2226

Yves-Michel Frapart – University of Paris Cité, CNRS, LCBPT, F-75006 Paris, France. https://orcid.org/0000-0003-3854-3580

Robert N. Muller – (1) NMR and Molecular Imaging Laboratory, General, Organic and Biomedical Chemistry Unit, University of Mons, B-7000 Mons, Belgium. (2) Center for Microscopy and Molecular Imaging (CMMI), B-6041 Gosselies, Belgium. https://orcid.org/0000-0001-8620-1804

## Conflicts of Interest

The authors have no relevant affiliations or financial involvement with any organization or entity with a financial interest in or financial conflict with the subject matter or materials discussed in the manuscript.

## Acknowledgments

The authors acknowledge P. Massot from the CNRS-UMR5536 and R. Abregel from MAP5-UMR 8145 for their invaluable assistance throughout the project. The authors thank the laboratories of J-M. Raquez for providing access to TGA equipment, P. Duez for the access to ICP-AES instrument and the Center for Microscopy and Molecular Imaging (CMMI, supported by the European Regional Development Fund and the Walloon Region). The authors are also grateful to Materia Nova for collaboration and support in the XPS characterizations. This work was supported by the Fond National de la Recherche Scientifique (FNRS), the ARC Programs of the French Community of Belgium, and the Walloon Region (Prother-Wal and Interreg projects).

## References

(1) Danhier, P.; Gallez, B. Electron Paramagnetic Resonance: A Powerful Tool to Support Magnetic Resonance Imaging Research. *Contrast Media Mol. Imaging* **2015**, *10* (4), 266–281. https://doi.org/10.1002/cmmi.1630.

(2) Kempe, S.; Metz, H.; Mäder, K. Application of Electron Paramagnetic Resonance (EPR) Spectroscopy and Imaging in Drug Delivery Research – Chances and Challenges. *Eur. J. Pharm. Biopharm.* **2010**, *74* (1), 55–66. https://doi.org/10.1016/j.ejpb.2009.08.007.

(3) Abbas, K.; Babić, N.; Peyrot, F. Use of Spin Traps to Detect Superoxide Production in Living Cells by Electron Paramagnetic Resonance (EPR) Spectroscopy. *Methods* **2016**, *109*, 31–43. https://doi.org/10.1016/j.ymeth.2016.05.001.

(4) Bordignon, E. EPR Spectroscopy of Nitroxide Spin Probes. In *eMagRes*; Harris, R. K., Wasylishen, R. L., Eds.; John Wiley & Sons, Ltd: Chichester, UK, 2017; pp 235–254. https://doi.org/10.1002/9780470034590.emrstm1513.
(5) Tran, D.-N.; Li-Thiao-Te, S.; Frapart, Y.-M. Parameter Estimation for Quantitative EPR Spectroscopy. *IEEE Trans. Instrum. Meas.* **2021**, *70*, 1–7. https://doi.org/10.1109/TIM.2021.3084289.
(6) Krishna, M. C.; Subramanian, S. The Development of Time-Domain In Vivo EPR Imaging at NCI. *Appl. Magn. Reson.* **2021**, *52* (10), 1291–1309. https://doi.org/10.1007/s00723-021-01369-4.
(7) Sahu, I. D.; Lorigan, G. A. Electron Paramagnetic Resonance as a Tool for Studying Membrane Proteins. *Biomolecules* **2020**, *10* (5), 763. https://doi.org/10.3390/biom10050763.
(8) Hofmann, L.; Ruthstein, S. EPR Spectroscopy Provides New Insights into Complex Biological Reaction Mechanisms. *J. Phys. Chem. B* **2022**, *126* (39), 7486–7494. https://doi.org/10.1021/acs.jpcb.2c05235.
(9) Galazzo, L.; Bordignon, E. Electron Paramagnetic Resonance Spectroscopy in Structural-Dynamic Studies of Large Protein Complexes. *Prog. Nucl. Magn. Reson. Spectrosc.* **2023**, *134–135*, 1–19. https://doi.org/10.1016/j.pnmrs.2022.11.001.
(10) Passeri, D.; Rinaldi, F.; Ingallina, C.; Carafa, M.; Rossi, M.; Terranova, M. L.; Marianecci, C. Biomedical Applications of Nanodiamonds: An Overview. *J Nanosci. Nanotechnol.* **2015**, *15* (2), 972–988. https://doi.org/10.1166/jnn.2015.9734.
(11) Chauhan, S.; Jain, N.; Nagaich, U. Nanodiamonds with Powerful Ability for Drug Delivery and Biomedical Applications: Recent Updates on in Vivo Study and Patents. *J. Pharm. Anal.* **2020**, *10* (1), 1–12. https://doi.org/10.1016/j.jpha.2019.09.003.
(12) Garifo, S.; Stanicki, D.; Ayata, G.; Muller, R. N.; Laurent, S. Nanodiamonds as Nanomaterial for Biomedical Field. *Front. Mater. Sci.* **2021**, *15* (3), 334–351. https://doi.org/10.1007/s11706-021-0567-3.
(13) Pichot, V.; Muller, O.; Seve, A.; Yvon, A.; Merlat, L.; Spitzer, D. Optical Properties of Functionalized Nanodiamonds. *Sci. Rep.* **2017**, *7* (1), 14086. https://doi.org/10.1038/s41598-017-14553-z.
(14) Ekimov, E. A.; Shiryaev, A. A.; Grigoriev, Y.; Averin, A.; Shagieva, E.; Stehlik, S.; Kondrin, M. V. Size-Dependent Thermal Stability and Optical Properties of Ultra-Small Nanodiamonds Synthesized under High Pressure. *Nanomater.* **2022**, *12* (3), 351. https://doi.org/10.3390/nano12030351.
(15) Turcheniuk, K.; Mochalin, V. N. Biomedical Applications of Nanodiamond (Review). *Nanotechnol.* **2017**, *28* (25), 252001. https://doi.org/10.1088/1361-6528/aa6ae4.
(16) Ansari, S. A.; Satar, R.; Jafri, M. A.; Rasool, M.; Ahmad, W.; Kashif Zaidi, S. Role of Nanodiamonds in Drug Delivery and Stem Cell Therapy. *Iran. J. Biotechnol.* **2016**, *14* (3), 130–141. https://doi.org/10.15171/ijb.1320.
(17) Krok, E.; Balakin, S.; Jung, J.; Gross, F.; Opitz, J.; Cuniberti, G. Modification of Titanium Implants Using Biofunctional Nanodiamonds for Enhanced Antimicrobial Properties. *Nanotechnol.* **2020**, *31* (20), 205603. https://doi.org/10.1088/1361-6528/ab6d9b.
(18) Singh, D.; Ray, S. A Short Appraisal of Nanodiamonds in Drug Delivery and Targeting: Recent Advancements. *Front. Nanotechnol.* **2023**, *5*, 1259648. https://doi.org/10.3389/fnano.2023.1259648.
(19) Wu, Y.; Alam, M. N. A.; Balasubramanian, P.; Ermakova, A.; Fischer, S.; Barth, H.; Wagner, M.; Raabe, M.; Jelezko, F.; Weil, T. Nanodiamond Theranostic for Light-Controlled Intracellular Heating and Nanoscale Temperature Sensing. *Nano. Lett.* **2021**, *21* (9), 3780–3788. https://doi.org/10.1021/acs.nanolett.1c00043.
(20) Panich, A. M.; Salti, M.; Goren, S. D.; Yudina, E. B.; Aleksenskii, A. E.; Vul', A. Y.; Shames, A. I. Gd(III)-Grafted Detonation Nanodiamonds for MRI Contrast Enhancement. *J.*

*Phys. Chem. C* **2019**, *123* (4), 2627–2631. https://doi.org/10.1021/acs.jpcc.8b11655.
(21) Panich, A. M.; Salti, M.; Prager, O.; Swissa, E.; Kulvelis, Y. V.; Yudina, E. B.; Aleksenskii, A. E.; Goren, S. D.; Vul', A. Ya.; Shames, A. I. PVP-coated Gd-grafted Nanodiamonds as a Novel and Potentially Safer Contrast Agent for in Vivo MRI. *Magn. Reson. Med.* **2021**, *86* (2), 935–942. https://doi.org/10.1002/mrm.28762.
(22) Kunuku, S.; Lin, B.-R.; Chen, C.-H.; Chang, C.-H.; Chen, T.-Y.; Hsiao, T.-Y.; Yu, H.-K.; Chang, Y.-J.; Liao, L.-C.; Chen, F.-H.; Bogdanowicz, R.; Niu, H. Nanodiamonds Doped with Manganese for Applications in Magnetic Resonance Imaging. *ACS Omega* **2023**, *8* (4), 4398–4409. https://doi.org/10.1021/acsomega.2c08043.
(23) Panich, A. M.; Shames, A. I.; Aleksenskii, A. E.; Yudina, E. B.; Vul', A. Ya. Manganese-Grafted Detonation Nanodiamond, a Novel Potential MRI Contrast Agent. *Diam. Relat. Mater.* **2021**, *119*, 108590. https://doi.org/10.1016/j.diamond.2021.108590.
(24) Panich, A. M.; Salti, M.; Aleksenskii, A. E.; Kulvelis, Y. V.; Chizhikova, A.; Vul', A. Ya.; Shames, A. I. Suspensions of Manganese-Grafted Nanodiamonds: Preparation, NMR, and MRI Study. *Diam. Relat. Mater.* **2023**, *131*, 109591. https://doi.org/10.1016/j.diamond.2022.109591.
(25) Garifo, S.; Vangijzegem, T.; Stanicki, D.; Laurent, S. A Review on the Design of Carbon-Based Nanomaterials as MRI Contrast Agents. *Mol.* **2024**, *29* (7), 1639. https://doi.org/10.3390/molecules29071639.
(26) Waddington, D. E. J.; Boele, T.; Rej, E.; McCamey, D. R.; King, N. J. C.; Gaebel, T.; Reilly, D. J. Phase-Encoded Hyperpolarized Nanodiamond for Magnetic Resonance Imaging. *Sci. Rep.* **2019**, *9* (1), 5950. https://doi.org/10.1038/s41598-019-42373-w.
(27) Waddington, D. E. J.; Sarracanie, M.; Zhang, H.; Salameh, N.; Glenn, D. R.; Rej, E.; Gaebel, T.; Boele, T.; Walsworth, R. L.; Reilly, D. J.; Rosen, M. S. Nanodiamond-Enhanced MRI via in Situ Hyperpolarization. *Nat. Commun.* **2017**, *8* (1), 15118. https://doi.org/10.1038/ncomms15118.
(28) Ajoy, A.; Nazaryan, R.; Druga, E.; Liu, K.; Aguilar, A.; Han, B.; Gierth, M.; Oon, J. T.; Safvati, B.; Tsang, R.; Walton, J. H.; Suter, D.; Meriles, C. A.; Reimer, J. A.; Pines, A. Room Temperature "*Optical Nanodiamond Hyperpolarizer*": Physics, Design, and Operation. *Rev. Sci. Instrum.* **2020**, *91* (2), 023106. https://doi.org/10.1063/1.5131655.
(29) Bobko, A. A.; Kirilyuk, I. A.; Grigor'ev, I. A.; Zweier, J. L.; Khramtsov, V. V. Reversible Reduction of Nitroxides to Hydroxylamines: Roles for Ascorbate and Glutathione. *Free Radic. Biol. Med.* **2007**, *42* (3), 404–412. https://doi.org/10.1016/j.freeradbiomed.2006.11.007.
(30) Jaymand, M.; Davatgaran Taghipour, Y.; Rezaei, A.; Derakhshankhah, H.; Foad Abazari, M.; Samadian, H.; Hamblin, M. R. Radiolabeled Carbon-Based Nanostructures: New Radiopharmaceuticals for Cancer Therapy? *Coord. Chem. Rev.* **2021**, *440*, 213974. https://doi.org/10.1016/j.ccr.2021.213974.
(31) Mochalin, V. N.; Shenderova, O.; Ho, D.; Gogotsi, Y. The Properties and Applications of Nanodiamonds. *Nat. Nanotechnol.* **2012**, *7* (1), 11–23. https://doi.org/10.1038/nnano.2011.209.
(32) Qin, J.-X.; Yang, X.-G.; Lv, C.-F.; Li, Y.-Z.; Liu, K.-K.; Zang, J.-H.; Yang, X.; Dong, L.; Shan, C.-X. Nanodiamonds: Synthesis, Properties, and Applications in Nanomedicine. *Mater. Des.* **2021**, *210*, 110091. https://doi.org/10.1016/j.matdes.2021.110091.
(33) Whitlow, J.; Pacelli, S.; Paul, A. Multifunctional Nanodiamonds in Regenerative Medicine: Recent Advances and Future Directions. *JCR* **2017**, *261*, 62–86. https://doi.org/10.1016/j.jconrel.2017.05.033.
(34) Kovářík, T.; Bělský, P.; Rieger, D.; Ilavsky, J.; Jandová, V.; Maas, M.; Šutta, P.; Pola, M.; Medlín, R. Particle Size Analysis and Characterization of Nanodiamond Dispersions in Water and Dimethylformamide by Various Scattering and Diffraction Methods. *J. Nanopart. Res.* **2020**, *22* (2), 34. https://doi.org/10.1007/s11051-020-4755-3.

(35) Stehlik, S.; Varga, M.; Ledinsky, M.; Jirasek, V.; Artemenko, A.; Kozak, H.; Ondic, L.; Skakalova, V.; Argentero, G.; Pennycook, T.; Meyer, J. C.; Fejfar, A.; Kromka, A.; Rezek, B. Size and Purity Control of HPHT Nanodiamonds down to 1 Nm. *J. Phys. Chem. C* **2015**, *119* (49), 27708–27720. https://doi.org/10.1021/acs.jpcc.5b05259.
(36) Rehor, I.; Cigler, P. Precise Estimation of HPHT Nanodiamond Size Distribution Based on Transmission Electron Microscopy Image Analysis. *Diam. Relat. Mater.* **2014**, *46*, 21–24. https://doi.org/10.1016/j.diamond.2014.04.002.
(37) Hannecart, A.; Stanicki, D.; Vander Elst, L.; Muller, R. N.; Brûlet, A.; Sandre, O.; Schatz, C.; Lecommandoux, S.; Laurent, S. Embedding of Superparamagnetic Iron Oxide Nanoparticles into Membranes of Well-Defined Poly(Ethylene Oxide)- *Block* -Poly(ε-Caprolactone) Nanoscale Magnetovesicles as Ultrasensitive MRI Probes of Membrane Bio-Degradation. *J. Mater. Chem. B* **2019**, *7* (30), 4692–4705. https://doi.org/10.1039/C9TB00909D.
(38) Schmidlin, L.; Pichot, V.; Comet, M.; Josset, S.; Rabu, P.; Spitzer, D. Identification, Quantification and Modification of Detonation Nanodiamond Functional Groups. *Diam. Relat. Mater.* **2012**, *22*, 113–117. https://doi.org/10.1016/j.diamond.2011.12.009.
(39) Volkov, D. S.; Proskurnin, M. A.; Korobov, M. V. Elemental Analysis of Nanodiamonds by Inductively-Coupled Plasma Atomic Emission Spectroscopy. *Carbon* **2014**, *74*, 1–13. https://doi.org/10.1016/j.carbon.2014.02.072.
(40) Stoll, S.; Schweiger, A. EasySpin, a Comprehensive Software Package for Spectral Simulation and Analysis in EPR. *J. Magn. Reson.* **2006**, *178* (1), 42–55. https://doi.org/10.1016/j.jmr.2005.08.013.
(41) Durand, S.; Frapart, Y.-M.; Kerebel, M. Electron Paramagnetic Resonance Image Reconstruction with Total Variation and Curvelets Regularization. *Inverse Probl.* **2017**, *33* (11), 114002. https://doi.org/10.1088/1361-6420/aa8412.
(42) Abergel, R.; Boussâa, M.; Durand, S.; Frapart, Y.-M. Electron Paramagnetic Resonance Image Reconstruction with Total Variation Regularization. *IPOL* **2023**, No. 13, 90–139. https://doi.org/10.5201/ipol.2023.414.
(43) Stehlik, S.; Mermoux, M.; Schummer, B.; Vanek, O.; Kolarova, K.; Stenclova, P.; Vlk, A.; Ledinsky, M.; Pfeifer, R.; Romanyuk, O.; Gordeev, I.; Roussel-Dherbey, F.; Nemeckova, Z.; Henych, J.; Bezdicka, P.; Kromka, A.; Rezek, B. Size Effects on Surface Chemistry and Raman Spectra of Sub-5 Nm Oxidized High-Pressure High-Temperature and Detonation Nanodiamonds. *J. Phys. Chem. C* **2021**, *125* (10), 5647–5669. https://doi.org/10.1021/acs.jpcc.0c09190.
(44) Dolmatov, V. Yu.; Lapchuk, N. M.; Lapchuk, T. M.; Nguyen, B. T. T.; Myllymäki, V.; Vehanen, A.; Yakovlev, R. Yu. A Study of Defects and Impurities in Doped Detonation Nanodiamonds by EPR, Raman Scattering, and XRD Methods. *J. Superhard Mater.* **2016**, *38* (4), 219–229. https://doi.org/10.3103/S1063457616040018.
(45) Shames, A. I.; Zegrya, G. G.; Samosvat, D. M.; Osipov, V. Y.; Vul', A. Y. Size Effect in Electron Paramagnetic Resonance Spectra of Impurity Centers in Diamond Particles. *Physica E Low Dimens. Syst. Nanostruct.* **2023**, *146*, 115523. https://doi.org/10.1016/j.physe.2022.115523.
(46) Panich, A. M.; Sergeev, N. A.; Shames, A. I.; Osipov, V. Y.; Boudou, J.-P.; Goren, S. D. Size Dependence of $^{13}$C Nuclear Spin-Lattice Relaxation in Micro- and Nanodiamonds. *J. Phys.: Condens. Matter.* **2015**, *27* (7), 072203. https://doi.org/10.1088/0953-8984/27/7/072203.
(47) Petit, T.; Puskar, L. FTIR Spectroscopy of Nanodiamonds: Methods and Interpretation. *Diam. Relat. Mater.* **2018**, *89*, 52–66. https://doi.org/10.1016/j.diamond.2018.08.005.
(48) Panich, A. M. Nuclear Magnetic Resonance Studies of Nanodiamonds. *Crit. Rev. Solid State Mater. Sci.* **2012**, *37* (4), 276–303. https://doi.org/10.1080/10408436.2011.606930.
(49) Mermoux, M.; Chang, S.; Girard, H. A.; Arnault, J.-C. Raman Spectroscopy Study of

Detonation Nanodiamond. *Diam. Relat. Mater.* **2018**, *87*, 248–260. https://doi.org/10.1016/j.diamond.2018.06.001.
(50) Zegrya, G. G.; Samosvat, D. M.; Osipov, V. Y.; Vul', A. Y.; Shames, A. I. Size Effect in Electron Paramagnetic Resonance Spectra of Impurity Centers in Diamond Nanoparticles. *Mesoscale Nanoscale Phys.* **2019**, 1–25. https://doi.org/10.48550/arXiv.1912.06330.
(51) Shames, A. I.; Panich, A. M.; Kempiński, W.; Alexenskii, A. E.; Baidakova, M. V.; Dideikin, A. T.; Osipov, V. Yu.; Siklitski, V. I.; Osawa, E.; Ozawa, M.; Vul', A. Ya. Defects and Impurities in Nanodiamonds: EPR, NMR and TEM Study. *J. Phys. Chem. Solids* **2002**, *63* (11), 1993–2001. https://doi.org/10.1016/S0022-3697(02)00185-3.
(52) Bézière, N.; Decroos, C.; Mkhitaryan, K.; Kish, E.; Richard, F.; Bigot-Marchand, S.; Durand, S.; Cloppet, F.; Chauvet, C.; Corvol, M.-T.; Rannou, F.; Xu-Li, Y.; Mansuy, D.; Peyrot, F.; Frapart, Y.-M. First Combined in Vivo X-Ray Tomography and High-Resolution Molecular Electron Paramagnetic Resonance (EPR) Imaging of the Mouse Knee Joint Taking into Account the Disappearance Kinetics of the EPR Probe. *Mol. Imaging* **2012**, *11* (3), 7290.2011.00042. https://doi.org/10.2310/7290.2011.00042.

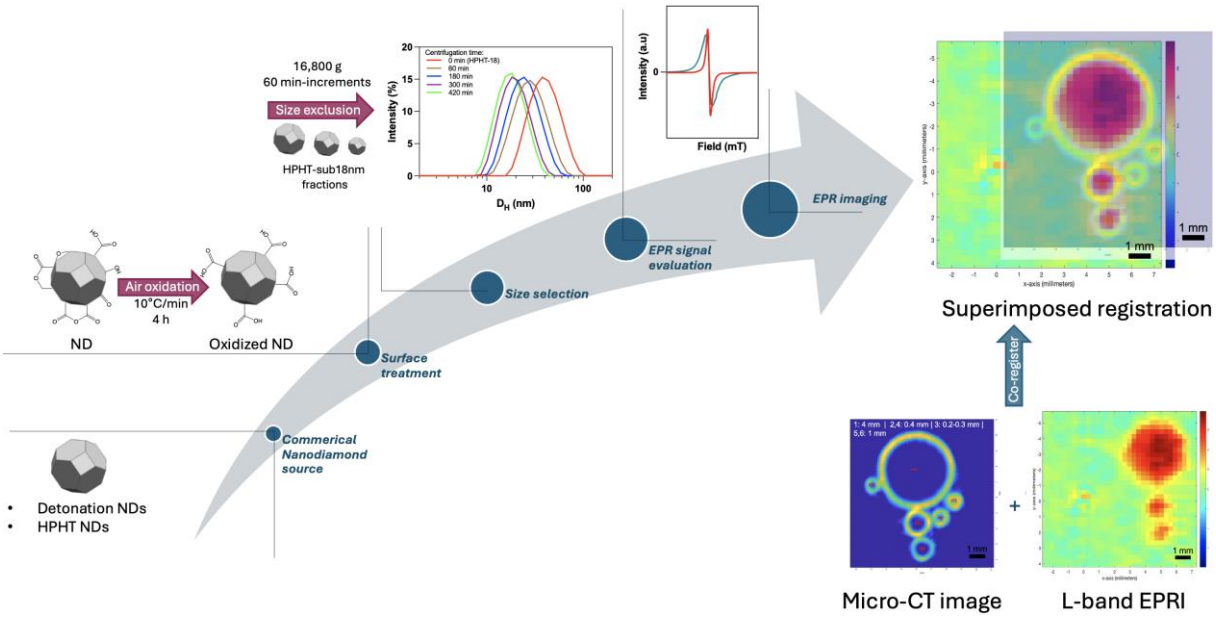


**Graphical abstract / TOCG**